university of groningen

University Medical Center Groningen

University of Groningen

On crystal plasticity FLD analysis

Wu, P.D.; Neale, K.W.; van der Giessen, E.

Published in:
Proceedings of the Royal Society of London Series A- Mathematical Physical and Engineering Sciences

DOI:
10.1098/rspa.1997.0099

IMPORTANT NOTE: You are advised to consult the publisher's version (publisher's PDF) if you wish to cite from it. Please check the document version below.

Document Version
Publisher's PDF, also known as Version of record

Publication date:
1997

Link to publication in University of Groningen/UMCG research database

Citation for published version (APA):
Wu, P. D., Neale, K. W., & van der Giessen, E. (1997). On crystal plasticity FLD analysis. *Proceedings of the Royal Society of London Series A- Mathematical Physical and Engineering Sciences*, *453*(1964), 1831 - 1848. https://doi.org/10.1098/rspa.1997.0099

Copyright
Other than for strictly personal use, it is not permitted to download or to forward/distribute the text or part of it without the consent of the author(s) and/or copyright holder(s), unless the work is under an open content license (like Creative Commons).

The publication may also be distributed here under the terms of Article 25fa of the Dutch Copyright Act, indicated by the “Taverne” license. More information can be found on the University of Groningen website: https://www.rug.nl/library/open-access/self-archiving-pure/taverne-amendment.

Take-down policy
If you believe that this document breaches copyright please contact us providing details, and we will remove access to the work immediately and investigate your claim.

Downloaded from the University of Groningen/UMCG research database (Pure): http://www.rug.nl/research/portal. For technical reasons the number of authors shown on this cover page is limited to 10 maximum.

Download date: 04-05-2023

On crystal plasticity FLD analysis

By P. D. Wu[1], K. W. Neale[1] and E. Van der Giessen[2]

[1] *University of Sherbrooke, Faculty of Applied Science, Sherbrooke, Quebec, Canada J1K 2R1*

[2] *Delft University of Technology, Laboratory for Engineering Mechanics, Mekelweg 2, 2628 CD Delft, The Netherlands*

This paper is concerned with the computation of forming limit diagrams (FLDs) using a rate-sensitive polycrystal plasticity model together with the Marciniak–Kuczynski approach. Sheet necking is initiated from an initial imperfection in terms of a narrow band. The deformations inside and outside the band are assumed to be homogeneous and conditions of compatibility and equilibrium are enforced across the band interfaces. Thus, the polycrystal model needs only to be applied to two polycrystalline aggregates, one inside and one outside the band. Each grain is modelled as an FCC crystal with 12 distinct slip systems. The response of an aggregate comprised of many grains is based on an elastic–viscoplastic Taylor-type polycrystal model developed by Asaro & Needleman in 1985. The effects of initial imperfection intensity and orientation, initial distribution of grain orientations, crystal elasticity, strain rate sensitivity, single slip hardening and latent hardening on the FLD are discussed in detail. The predicted FLD is compared with experimental data for an aluminium alloy sheet.

1. Introduction

The forming limit diagram (FLD) concept has proved to be extremely useful for representing conditions for the onset of sheet necking (e.g. Hecker 1975), and is now a standard tool for characterizing materials in terms of their drawability. Past studies have clearly established that predictions of FLDs depend on numerous parameters. There is thus a considerable need to analyse the influence of each parameter on the FLD in order to improve and optimize the sheet forming process. However, it is difficult to experimentally assess the influence of each parameter individually since it is virtually impossible to change only one at a time. Furthermore, experiments on FLDs are time consuming and expensive relative to numerical simulations. Therefore, reliable theoretical analyses and numerical simulations for FLDs turn out to be of great practical importance.

Theoretical calculations of FLDs were initially based on Hill's criterion for localized necking along a direction of zero extension (Hill 1952). However, when a sheet is deformed by biaxial tension so that both principal strain increments in the plane of the sheet are positive ($d\varepsilon_2/d\varepsilon_1 = \rho > 0$), there is no line of zero extension in the plane, and the description of localized necking given by Hill (1952) does not predict the onset of localized necking.

Marciniak & Kuczynski (1967), by introducing a thickness imperfection of infinite length normal to the principal stress direction, developed the first analytical

Proc. R. Soc. Lond. A (1997) **453**, 1831–1848
Printed in Great Britain

© 1997 The Royal Society
TEX Paper

model (hereafter referred to as the M–K approach) to predict localized necking in biaxial stretching ($\rho > 0$) of sheets. They showed that the presence of even slight intrinsic inhomogeneities in load bearing capacity throughout a deforming sheet can lead to unstable growth of strain in the weaker regions, and subsequently lead to localized necking and failure. Within this framework, the influence of various constitutive features on FLDs has been explored using phenomenological plasticity models (e.g. Chan 1989; Ferron & Molinari 1989). It is now well known that the FLD is very sensitive to, amongst other things, effects of yield surface vertices, anisotropy and material rate sensitivity (e.g. Hutchinson & Neale 1978; Stören & Rice 1978; Bassani *et al.* 1979). For instance, a slight change of the shape of the yield surface for a sheet metal can result in a large variation of its FLD (Neale & Chater 1980; Lian *et al.* 1989). Since the mechanical properties of a sheet metal are determined by its microstructure and microscopic properties, the FLD based on phenomenological models remains a diagnostic tool rather than a predictive one because phenomenological models cannot account for the effects of microstructure and its evolution with deformation. Crystallographic texture is usually the prime feature of microstructural evolution in sheet metals. To incorporate this, crystal plasticity FLD analyses are required.

Bassani *et al.* (1979) and Barlat and co-workers (Barlat 1987, 1989; Barlat & Richmond 1987) calculated a series of Bishop–Hill yield surfaces of polycrystals corresponding to various crystallographic textures. They obtained, in certain cases, FLDs which are in good agreement with the corresponding experimental observations (Lege *et al.* 1989). However, Bassani *et al.* (1979) and Barlat and co-workers have not considered the subsequent evolution of the yield surface during deformation, nor the effect of elasticity. Zhou & Neale (1995) have directly applied a rate-sensitive crystal plasticity model in conjunction with the M–K approach to predict FLDs for annealed FCC sheet metals. The initial texture and its evolution were considered in their analyses. However, elasticity was neglected and the imperfection groove was restricted to be normal to the major principal stretch direction. The effect of elasticity was considered by Qiu *et al.* (1995), but again, the influence of groove orientation was not assessed in their analyses. Using their elastic–viscoplastic Taylor-type polycrystal model, Asaro & Needleman (1985) and later on Tvergaard & Needleman (1993) calculated the forming limit strains only for equal-biaxial stretching ($\rho = 1$) and in-plane plane-strain stretching ($\rho = 0$), rather than the full FLDs.

In this paper, the polycrystal plasticity model developed by Asaro & Needleman (1985) is directly used in a nonlinear numerical solution to calculate the FLDs for FCC polycrystals. This approach too is based on the M–K approach; that is, sheet necking is initiated from an initial imperfection represented in terms of a narrow band, with the deformations inside and outside the band being homogeneous. Thus, the rather complex polycrystal model needs only to be applied to two separate stress–strain histories, one inside and one outside the band. The conditions of compatibility and equilibrium are enforced across the band interfaces. Each grain is modelled as an FCC crystal with 12 distinct slip systems. The response of an aggregate comprised of many grains is based on the elastic–viscoplastic Taylor-type polycrystal model of Asaro & Needleman (1985). Since the deformations are assumed to be uniform both inside and outside the band, the computational requirements are relatively modest. Therefore, the influence of the various model parameters on the FLD can be assessed.

The plan of this paper is as follows. In § 2, we briefly recapitulate the constitutive model. The problem formulation and the method of solution are presented in § 3. We

begin § 4 by giving a calculated FLD for a typical aluminium alloy sheet. The effects of initial imperfection intensity and orientation, initial distribution of grain orientations, crystal elasticity, strain rate sensitivity, single slip hardening and latent hardening on the FLD are also discussed in § 4. We complete § 4 by comparing the predicted FLD with the experimental data for an aluminium alloy sheet. The discussion and conclusions are presented in § 5.

Tensors and vectors will be denoted by bold face letters. The tensor product is denoted by $\otimes$ and the following operation for second-order tensors applies ($\boldsymbol{a} = a_{ij}\boldsymbol{e}_i \otimes \boldsymbol{e}_j$, $\boldsymbol{b} = b_{ij}\boldsymbol{e}_i \otimes \boldsymbol{e}_j$, $\boldsymbol{e}_i$ being a Cartesian basis): $\boldsymbol{ab} = a_{ik}b_{kj}\boldsymbol{e}_i \otimes \boldsymbol{e}_j$, $\boldsymbol{a} \cdot \boldsymbol{b} = a_{ij}b_{ij}$, with proper extension to high-order tensors. Superscripts T and -1 denote the transverse and inverse of a second-order tensor, respectively. The trace is denoted by tr. Furthermore, the range of Greek tensor indices $\alpha, \beta = 1, 2$, while italic indices run from 1 to 3.

2. Constitutive model

We start by briefly recapitulating the constitutive model employed in this paper. For details, we refer to Asaro & Needleman (1985).

The total deformation of a crystallite is the result of two distinct physical mechanisms: crystallographic slip due to dislocation motion on the active slip systems, and elastic lattice distortion. We consider FCC crystals having the usual $\{111\}\langle 110\rangle$ slip systems where the slip planes are the $\{111\}$ crystallographic planes with normals $\boldsymbol{m}$, and the $\langle 110\rangle$ directions are shear directions with slip vectors $\boldsymbol{s}$. Plastic deformation of the crystal is envisaged to occur as a set of plastic simple shears along the various slip systems, leaving the lattice and the slip systems' vectors ($\boldsymbol{s}_{(\alpha)}$, $\boldsymbol{m}_{(\alpha)}$) not only essentially undistorted, but also unrotated (the brackets in the subscripts (α) indicate that α is not a tensor index and ranges from one to the number of slip systems). Next, the material and lattice are considered to deform elastically and rotate rigidly from the plastically deformed state to the current configuration. Accordingly, we have the following decomposition for the deformation gradient tensor $\boldsymbol{F}$:

$$\boldsymbol{F} = \boldsymbol{F}^*\boldsymbol{F}^{\mathrm{p}}, \tag{2.1}$$

where $\boldsymbol{F}^{\mathrm{p}}$ consists solely of crystallographic slipping along specific slip systems, and $\boldsymbol{F}^*$ arises from the stretching and rotation of the crystal lattice. From (2.1), the spatial gradient of velocity can be written as

$$\boldsymbol{L} = \dot{\boldsymbol{F}}\boldsymbol{F}^{-1} = \boldsymbol{L}^* + \boldsymbol{L}^{\mathrm{p}}, \tag{2.2}$$

where

$$\boldsymbol{L}^* = \dot{\boldsymbol{F}}^*\boldsymbol{F}^{-1}, \quad \boldsymbol{L}^{\mathrm{p}} = \boldsymbol{F}^*(\dot{\boldsymbol{F}}^{\mathrm{p}}\boldsymbol{F}^{\mathrm{p}-1})\boldsymbol{F}^{*-1}. \tag{2.3}$$

Taking symmetric and antisymmetric parts of the above relations leads to the elastic and plastic strain rate $\boldsymbol{D}^*$ and $\boldsymbol{D}^{\mathrm{p}}$, the so-called plastic spin $\boldsymbol{W}^{\mathrm{p}}$ and the spin $\boldsymbol{W}^*$ associated with the rigid lattice rotation:

$$\boldsymbol{D} = \boldsymbol{D}^* + \boldsymbol{D}^{\mathrm{p}}, \quad \boldsymbol{W} = \boldsymbol{W}^* + \boldsymbol{W}^{\mathrm{p}}. \tag{2.4}$$

Since $\boldsymbol{s}_{(\alpha)}$ and $\boldsymbol{m}_{(\alpha)}$ are regarded as lattice vectors, they are stretched and rotated as follows:

$$\boldsymbol{s}^*_{(\alpha)} = \boldsymbol{F}^*\boldsymbol{s}_{(\alpha)}, \quad \boldsymbol{m}^*_{(\alpha)} = \boldsymbol{m}_{(\alpha)}\boldsymbol{F}^{*-1}.$$

The vectors $\boldsymbol{s}^*_{(\alpha)}$ and $\boldsymbol{m}^*_{(\alpha)}$, orthogonal since $\boldsymbol{s}_{(\alpha)}$ and $\boldsymbol{m}_{(\alpha)}$ are, characterize a particular slip system in the current state, and their evolution is governed by

$$\dot{\boldsymbol{s}}^*_{(\alpha)} = \boldsymbol{L}^* \boldsymbol{s}^*_{(\alpha)}, \quad \dot{\boldsymbol{m}}^*_{(\alpha)} = -\boldsymbol{L}^{*T} \boldsymbol{m}^*_{(\alpha)}.$$

By introducing for each slip system, α, the following symmetric and skewsymmetric tensors:

$$\boldsymbol{P}_{(\alpha)} = \operatorname{sym}(\boldsymbol{s}^*_{(\alpha)} \otimes \boldsymbol{m}^*_{(\alpha)}), \quad \boldsymbol{W}_{(\alpha)} = \operatorname{skew}(\boldsymbol{s}^*_{(\alpha)} \otimes \boldsymbol{m}^*_{(\alpha)}), \tag{2.5}$$

respectively, the plastic strain rate and spin for the crystal can be written as

$$\boldsymbol{D}^{\mathrm{p}} = \sum_{\alpha} \boldsymbol{P}_{(\alpha)} \dot{\gamma}_{(\alpha)}, \quad \boldsymbol{W}^{\mathrm{p}} = \sum_{\alpha} \boldsymbol{W}_{(\alpha)} \dot{\gamma}_{(\alpha)}, \tag{2.6}$$

where $\dot{\gamma}_{(\alpha)}$ is the shear rate on the slip system α. The elastic constitutive equation for a crystal is specified by

$$\overset{\nabla}{\boldsymbol{\tau}}{}^* = \dot{\boldsymbol{\tau}} - \boldsymbol{W}^* \boldsymbol{\tau} + \boldsymbol{\tau} \boldsymbol{W}^* = \mathcal{L} \boldsymbol{D}^*, \tag{2.7}$$

where $\overset{\nabla}{\boldsymbol{\tau}}{}^*$ is the Jaumann rate of the Kirchhoff stress tensor $\boldsymbol{\tau}$ based on the lattice rotations, and $\mathcal{L}$ is the tensor of elastic moduli. These moduli are based on the anisotropic elastic constants of the FCC crystal and thus exhibit the appropriate cubic symmetry.

In order to express the constitutive equation (2.7) in terms of the Jaumann rate $\overset{\nabla}{\boldsymbol{\sigma}}$ of Cauchy stress $\boldsymbol{\sigma} = \det(\boldsymbol{F})^{-1} \boldsymbol{\tau}$, based on the continuum spin $\boldsymbol{W}$, we introduce a second-order tensor $\boldsymbol{R}_{(\alpha)}$ for each slip system as follows:

$$\boldsymbol{R}_{(\alpha)} = \mathcal{L} \boldsymbol{P}_{(\alpha)} + \boldsymbol{W}_{(\alpha)} \boldsymbol{\sigma} - \boldsymbol{\sigma} \boldsymbol{W}_{(\alpha)}. \tag{2.8}$$

Using (2.4)–(2.6) and (2.8), the constitutive equation (2.7) can be rewritten in the form

$$\overset{\nabla}{\boldsymbol{\sigma}} = \mathcal{L} \boldsymbol{D} - \dot{\boldsymbol{\sigma}}^0 - \boldsymbol{\sigma} \operatorname{tr} \boldsymbol{D}, \tag{2.9}$$

where $\dot{\boldsymbol{\sigma}}^0$ is a viscoplastic-type stress rate defined by

$$\dot{\boldsymbol{\sigma}}^0 = \sum_{\alpha} \boldsymbol{R}_{(\alpha)} \dot{\gamma}_{(\alpha)}. \tag{2.10}$$

The slip rates to be substituted into (2.10) are taken to be governed by the power-law expression

$$\dot{\gamma}_{(\alpha)} = \dot{\gamma}_0 \operatorname{sgn} \tau_{(\alpha)} \left| \frac{\tau_{(\alpha)}}{g_{(\alpha)}} \right|^{1/m}, \tag{2.11}$$

where $\tau_{(\alpha)}$ is the resolved shear stress on slip system α:

$$\tau_{(\alpha)} = \boldsymbol{P}_{(\alpha)} \cdot \boldsymbol{\sigma}, \tag{2.12}$$

and $g_{(\alpha)}$ is its hardness; m is the strain-rate sensitivity index and $\dot{\gamma}_0$ is a reference shear rate.

The $g_{(\alpha)}$ characterize the current strain hardened state of the crystal. For multiple slip, the evolution of the hardness is taken to be governed by

$$\dot{g}_{(\alpha)} = \sum_{\beta} h_{(\alpha\beta)} |\dot{\gamma}_{(\beta)}|, \tag{2.13}$$

where $g_{(\alpha)}(0)$ is the initial hardness and is taken to be a constant τ_0 for each slip system, and where $h_{(\alpha\beta)}$ are the hardening moduli. The form of the moduli is

$$h_{(\alpha\beta)} = q_{(\alpha\beta)} h_{(\beta)} \quad (\text{no sum on } \beta), \tag{2.14}$$

where $h_{(\beta)}$ is a single slip hardening rate, and $q_{(\alpha\beta)}$ is the matrix describing the latent hardening behaviour of the crystallite. For FCC crystals with 12 slip systems, we take $q_{(\alpha\beta)}$ to be given by (Asaro & Needleman 1985)

$$q_{(\alpha\beta)} = \begin{bmatrix} \boldsymbol{A} & q\boldsymbol{A} & q\boldsymbol{A} & q\boldsymbol{A} \\ q\boldsymbol{A} & \boldsymbol{A} & q\boldsymbol{A} & q\boldsymbol{A} \\ q\boldsymbol{A} & q\boldsymbol{A} & \boldsymbol{A} & q\boldsymbol{A} \\ q\boldsymbol{A} & q\boldsymbol{A} & q\boldsymbol{A} & \boldsymbol{A} \end{bmatrix}$$

where q is the ratio of the latent hardening rate to self hardening rate, and $\boldsymbol{A}$ is a 3×3 matrix fully populated by ones. In the above, the numbering is taken to be such that slip systems $\{1, 2, 3\}$ are coplanar, as are systems $\{4, 5, 6\}$, $\{7, 8, 9\}$ and $\{10, 11, 12\}$. Thus the ratio of the latent hardening rate to the self hardening rate for coplanar systems is taken as unity.

Asaro & Needleman (1985), among others, simply take each $g_{(\alpha)}$ to depend on the accumulated sum, γ_{a}, of the slips; i.e.

$$g_{(\alpha)} = g_{(\alpha)}(\gamma_{\mathrm{a}}), \quad \gamma_{\mathrm{a}} = \int_0^t \sum_{\alpha} |\dot{\gamma}_{(\alpha)}| \, \mathrm{d}t. \tag{2.15}$$

Thus, $h_{(\beta)}$ is identical for each system β.

The single slip hardening law employed in this paper takes the following power-law form of the constitutive function $h_{(\beta)}$

$$h_{(\beta)} = h_0 \left(\frac{h_0 \gamma_{\mathrm{a}}}{\tau_0 n} + 1 \right)^{n-1}, \tag{2.16}$$

where h_0 is the system's initial hardening rate.

The response of a polycrystal comprised of many grains is obtained by invoking the Taylor assumption. Thus, at a material point representing a polycrystal of N grains, the deformation in each grain is taken to be identical to the macroscopic deformation of the continuum. Furthermore, the macroscopic values of all quantities, such as stresses, stress rates and elastic moduli, are obtained by averaging their respective values over the total number of grains at the particular material point.

3. Problem formulation and method of solution

The FLD analysis is applied to polycrystalline sheets having orthotropic textures. The axes x_1 and x_2 define the directions of orthotropy in the plane of the sheet, while x_3 represents the direction normal to the sheet. In the numerical simulations, textures satisfying these conditions of orthotropy will be employed.

We consider a sheet having a non-uniformity in the form of a groove or band which is initially inclined at an angle ψ_{I} with respect to the x_1 direction (figure 1). Tensor components are taken with reference to the Cartesian x_i coordinate system. Quantities inside the band are denoted by $(\,)^{\mathrm{b}}$. The thickness along the minimum section in the band is denoted by $h^{\mathrm{b}}(t)$, with an initial value $h^{\mathrm{b}}(0)$. The initial geometric non-uniformity is defined by

$$f = h^{\mathrm{b}}(0)/h(0), \tag{3.1}$$

where $h(0)$ is the initial thickness outside the band.

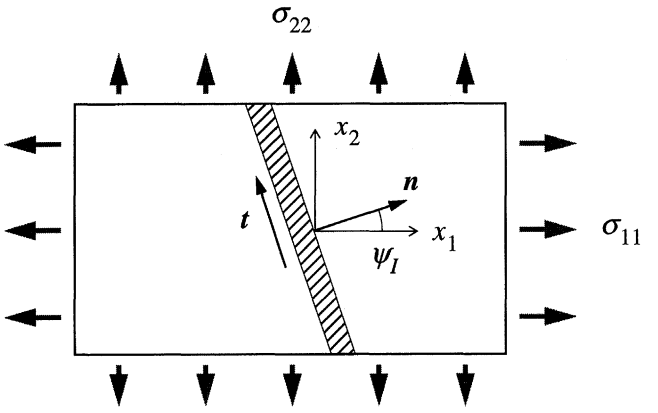

Figure 1. Thin sheet with an initial thickness imperfection initially inclined at an angle ψ_{I}.

The loading imposed on the edges of the sheet is assumed to be such that

$$\frac{D_{22}}{D_{11}} = \frac{\dot{\varepsilon}_{22}}{\dot{\varepsilon}_{11}} = \rho = \text{const.}, \quad D_{12} = 0, \quad W_{\alpha\beta} = 0, \tag{3.2}$$

where $\dot{\varepsilon}_{22}$ and $\dot{\varepsilon}_{11}$ are the (principal) logarithmic strain rates. We take $0 < \rho < 1$ so that in all cases ε_{11} is the major principal strain. We further assume that $D_{13} = D_{23} = W_{13} = W_{23} = 0$, while D_{33} is specified by the condition $\dot{\sigma}_{33} = 0$. For the orthotropic textures considered, these boundary conditions imply that the average stress components $\sigma_{13} = \sigma_{23} = 0$.

For the above deformation conditions, the current groove orientation ψ is given by

$$\tan\psi = \exp[(1-\rho)\varepsilon_{11}]\tan\psi_{\mathrm{I}}. \tag{3.3}$$

Since uniform deformations are assumed both inside and outside the band, equilibrium and compatibility inside and outside the band are automatically satisfied, apart from the necessary conditions at the band interface. Following Hutchinson & Neale (1978), the compatibility condition at the band interface is given in terms of the differences in the velocity gradients inside and outside the band

$$L^{\mathrm{b}}_{\alpha\beta} = L_{\alpha\beta} + \dot{c}_\alpha n_\beta, \tag{3.4}$$

or

$$D^{\mathrm{b}}_{\alpha\beta} = D_{\alpha\beta} + \tfrac{1}{2}(\dot{c}_\alpha n_\beta + n_\alpha \dot{c}_\beta), \quad W^{\mathrm{b}}_{\alpha\beta} = W_{\alpha\beta} + \tfrac{1}{2}(\dot{c}_\alpha n_\beta - n_\alpha \dot{c}_\beta). \tag{3.5}$$

Here, $n_1 = \cos\psi$ and $n_2 = \sin\psi$ are the components of the unit normal to the band in the current configuration, and $\dot{c}_\alpha$ are parameters to be determined. Equilibrium requires balance on each side of the interface so that

$$n_\alpha \sigma^{\mathrm{b}}_{\alpha\beta} h^{\mathrm{b}} = n_\alpha \sigma_{\alpha\beta} h, \tag{3.6}$$

in the current configuration. Now, a set of incremental equations for $\dot{c}_\alpha$ are obtained by substituting the incremental constitutive relations (2.9) into the incremental form of (3.6), using (3.5) to eliminate the strain increments $D^{\mathrm{b}}_{\alpha\beta}$. Together with the condition $\dot{\sigma}^{\mathrm{b}}_{33} = 0$, this furnishes three algebraic equations for solving $\dot{c}_1$, $\dot{c}_2$ and the unknown D^{b}_{33}.

The solution is obtained numerically by a linear incremental procedure. At any given stage of the prescribed strain path, the moduli $\mathcal{L}$ and $\dot{\boldsymbol{\sigma}}^0$ in (2.9) are calculated

for all grains inside and outside the band, by updating from the previous increment. The corresponding moduli and the visco-plastic type stress rates for the polycrystals representing materials inside and outside the band, are obtained by averaging over all grains inside and outside the band, respectively. Therefore, the rates $\dot{c}_\alpha$, or $D^{\mathrm{b}}_{\alpha\beta}$, and D^{b}_{33} inside the band are directly calculated by solving the three above-mentioned algebraic equations. The sheet thickness outside the band h and inside the band h^{b} are updated based on the rates

$$\dot{h} = D_{33}h, \quad \dot{h}^{\mathrm{b}} = D^{\mathrm{b}}_{33}h^{\mathrm{b}}. \tag{3.7}$$

For numerical stability, the polycrystal constitutive equations are implemented via the one-step explicit rate-tangent method described by (Peirce *et al.* 1983). Moreover, an adaptive time-stepping method developed by Van der Giessen & Neale (1993) is used. Finally, an equilibrium correction procedure is applied to prevent drifting of the solution from the true equilibrium path.

The onset of sheet necking is defined by the occurrence of a much higher maximum principal logarithmic strain rate inside the band than outside, in this case we employ the condition $\dot{\varepsilon}^{\mathrm{b}}/D_{11} \geqslant 10^5$. The corresponding principal logarithmic strains ε^*_{11} and ε^*_{22} outside the band are the limit strains. For a real sheet material, numerous initial imperfections exist with different orientations, resulting from surface roughness (Barlat 1989) or from microvoids in the materials (Wilson *et al.* 1981). The most conservative estimate of a forming limit strain is obtained by calculating the limit strain for various values of the chosen initial groove orientation and selecting the minimum limit strain as the predicted forming limiting strain. The entire FLD of a sheet is determined by repeating the procedure for different strain paths outside the band as prescribed by the value of ρ.

4. Results

Since most sheet forming operations are carried out on rolled materials, it is important for a numerical tool to be able to accurately predict FLDs for sheet metals with strong initial rolling textures. Consequently, we consider a typical rolled aluminium alloy sheet with its initial texture represented by the {111} stereographic pole figure shown in figure 2*a*. For the purpose of comparison, we also include results for a sheet with initially random texture shown in figure 2*b*. For the initially textured sheet 408 grains are used to represent the texture, while for the initially random sheet 300 grains are employed. Furthermore, we assume that, throughout this paper, the rolling direction (RD) is aligned to the major strain direction (x_1).

(*a*) *A typical FLD*

Figure 3 shows the predicted FLD for the rolled sheet with the initial texture shown in figure 2*a*. The simulation is carried out for an initial imperfection intensity $f = 0.99$. The crystal elastic constants are taken to be $C_{11} = 206$ GPa, $C_{12} = 118$ GPa and $C_{44} = 54$ GPa. The slip system reference plastic shearing rate is assumed to be $\dot{\gamma}_0 = 0.001s^{-1}$, while the slip rate sensitivity parameter $m = 0.002$. The values of the hardening parameters are $\tau_0 = 22$ MPa, $h_0/\tau_0 = 181.82$, $n = 0.16$ and $q = 1.0$. These values of material parameters are in the range of those for rolled aluminium sheets, and will be used in all simulations reported in this paper except where noted otherwise. It is seen from figure 3 that the predicted major limit strain ε^*_{11} decreases with ρ to reach its lowest point at $\rho = 0.20$, and then increases until $\rho = 0.6$. With

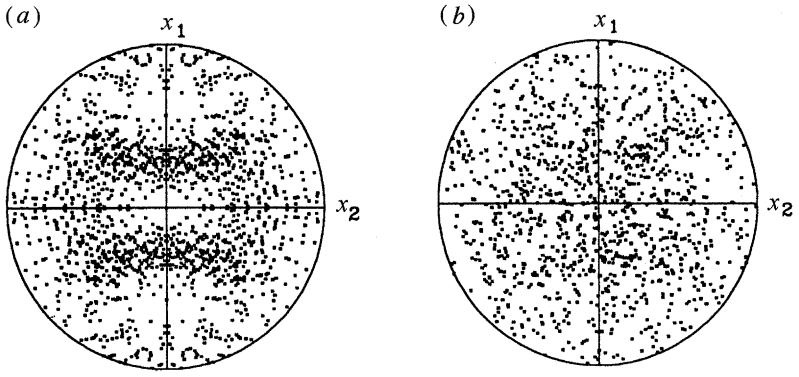

Figure 2. Initial grain orientation distributions represented by {111} stereographic pole figure for: (*a*) a sheet with a typical rolling texture; and (*b*) an initially random sheet.

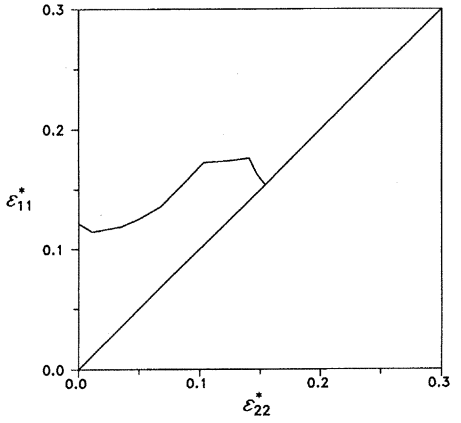

Figure 3. Typical predicted FLD for an initially textured sheet (as shown in figure 2*a*).

further increasing ρ, ε^*_{11} once again decreases. It is noted that the dip, near in-plane plane-strain tension ($\rho \leqslant 0.2$), in the predicted FLD is small but nevertheless significant, and has been observed experimentally (e.g. Ratchev *et al.* 1994).

(*b*) *Effects of initial imperfection*

If there is no initial imperfection ($f = 0$), the equations for $\dot{c}_\alpha$ and D^{b}_{33} are homogeneous, so that localization can only occur at a bifurcation point, and the first critical bifurcation of this type coincides with loss of ellipticity of the equations governing incremental equilibrium (Hill 1962; Rice 1977). For a rate-sensitive material as we consider in this paper, bifurcations into a localized mode are entirely governed by elasticity, and such bifurcations are not predicted at realistic stress levels (Tvergaard & Needleman 1993). Thus, the FLD prediction for elastic–viscoplastic materials relies on the gradual amplification of initial inhomogeneities.

Figure 4*a* shows the effects of initial imperfection on the predicted FLDs for the same initial texture and material parameters as before. As expected, the smaller the initial imperfection f, the larger the critical strain for sheet necking. For $\rho < 0.5$ or so, the effect is smaller than for larger ρ, but in both regimes the effect is rather insensitive to the precise value of ρ. It should be noted that in the simulations we have scanned every 5° of a range of ψ_{I} and then determined the critical groove angle that gives the minimum localization strain, i.e. the limit strain. Figure 4*b* gives the

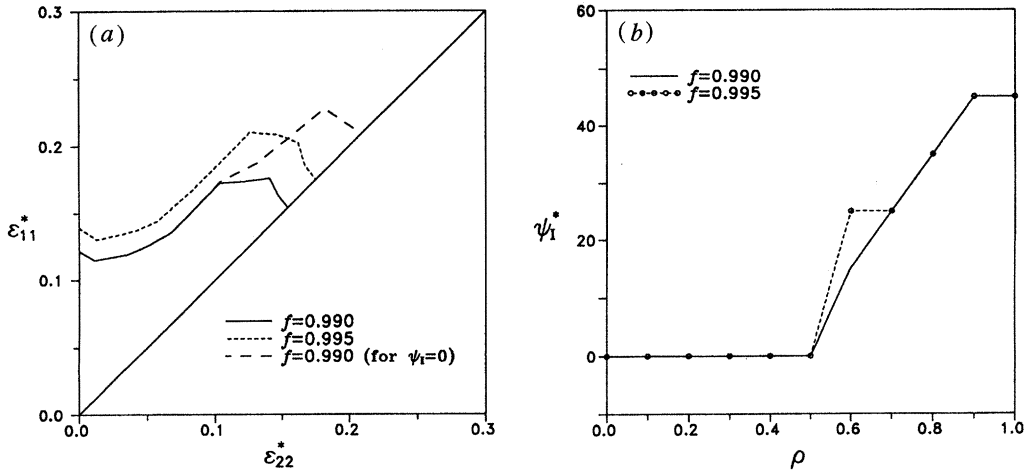

Figure 4. Influence of the initial imperfection f on: (*a*) the predicted FLDs; and (*b*) the predicted critical groove orientations for an initially textured sheet.

predicted critical groove orientations. It is seen that a groove oriented at $\psi_I = 0$ is favourable for necking when $\rho \leqslant 0.5$, while the critical groove orientation increases from 0 at $\rho = 0.5$–45° at balanced biaxial tension ($\rho = 1$). This effect of groove orientation can be also observed in figure 4*a*, where a case with groove orientations restricted to $\psi_I = 0$ is also included. The critical groove orientation is not very sensitive to the initial imperfection f in the range considered, bearing in mind that a predicted ψ_I^* is accurate to within 5°. It seems that one could overestimate the predicted limit strain, at least near balanced biaxial tension, for a rolled sheet with an initial texture as that shown in figure 2*a*, if one restricts the groove orientation to $\psi_I = 0$ in the FLD analysis, as was done by Zhou & Neale (1995) and by Qiu *et al.* (1995).

(*c*) *Effects of initial texture*

It is now well known that a slight change of the shape of the yield surface for a sheet metal can have a rather large effect on its FLD (Neale & Chater 1980; Lian *et al.* 1989). In the crystal plasticity FLD analysis carried out here, the shape of the 'yield surface' for a sheet metal is specified by the initial texture and its evolution. Consequently, the initial texture is one of the most important parameters effecting the FLDs.

Figure 5 represents a comparison between the predicted FLDs for an initially textured sheet (see figure 2*a*) and for an initially random sheet (see figure 2*b*), respectively. It is clear that the predicted shapes of FLDs are quite different. The predicted major limit strain ε_{11}^* for the initially random sheet is above that for the initially textured sheet when $\rho \leqslant 0.55$, while this trend is opposite when ρ are larger. It is noted that the predicted limit strains for the initially random sheet are not sensitive to the groove orientations.

(*d*) *Effects of material properties*

Previous studies with phenomenological models have indicated that FLDs are usually sensitive to effects of material properties such as strain hardening and material rate sensitivity (e.g. Hutchinson & Neale 1978; Zhou & Neale 1995). In this section,

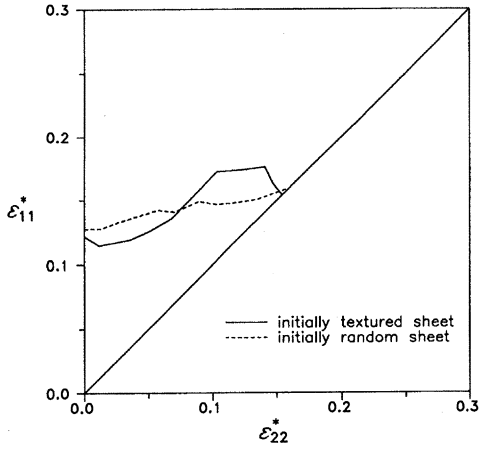

Figure 5. Influence of initial texture on the predicted FLDs.

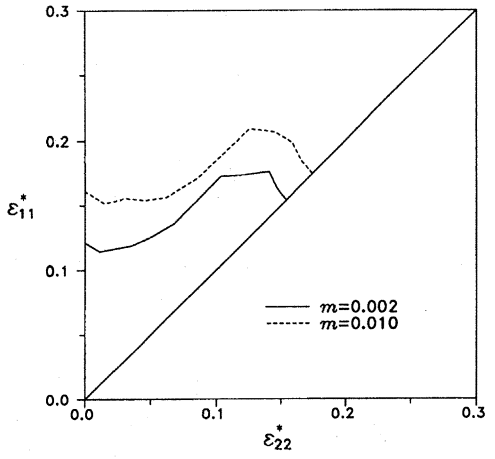

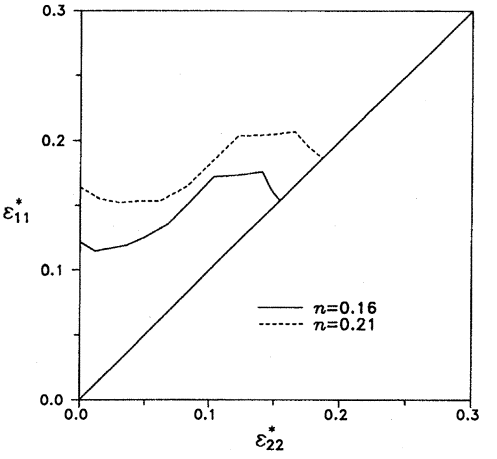

Figure 6. (Left) Influence of the material rate sensitivity parameter m on the predicted FLDs for an initially textured sheet.

Figure 7. (Right) Influence of the hardening parameter, n, on the predicted FLDs for an initially textured sheet.

we will examine systematically the effects of the material parameters in the present crystal plasticity model.

Figure 6 shows the change in the predicted FLD when the value of the material rate sensitivity m is increased by a factor five to $m = 0.01$. Increasing the rate sensitivity in (2.11) tends to enhance the hardening at large shears. Consistent with this, we see from figure 6 that the limit strain is increased relative to that in figure 3. The predicted critical groove orientations are found to be insensitive to m. It should be noted though that the tendency for texture development usually diminishes with increasing rate sensitivity. Consequently, the effect of m may vary with the strain path as different textures develop, but apparently the difference in texture evolutions between $m = 0.002$ and 0.01 remain small enough that this does not occur with the present parameters.

The parameters n, q and h_0 govern the strain hardening through the power-law expression. It is known that the effect of the parameter h_0 on material response is noticeable only when the applied strains are very small, and has no significant

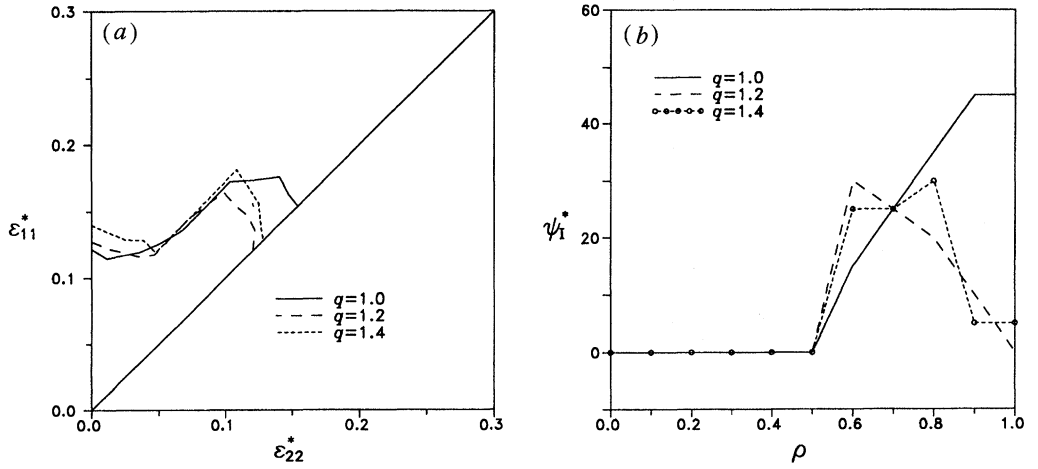

Figure 8. Influence of the latent hardening parameter q on: (*a*) the predicted FLDs; and (*b*) the predicted critical groove orientations for an initially textured sheet.

influence on FLDs. In figure 7, we study the effect of hardening by first using the same value of q ($q = 1.0$) but different values of n: $n = 0.16$ and 0.21. It is clearly seen that a larger value of n increases the limit strain, which can be attributed simply to the fact that hardening increases with increasing n. Consistent with this, the predicted critical groove orientations for the two n values are very close.

We proceed by studying the effect of the hardening characteristics by using the same value of n ($n = 0.16$) but different values of q: $q = 1.0$, 1.2 and 1.4. The predicted FLDs are presented in figure 8*a*. It is observed that increasing q increases the limit strain when $\rho \leqslant 0.4$ or so. The latent hardening effect ($q > 1.0$) decreases the limit strain near balanced biaxial tension. However, the predicted limit strain based on $q = 1.2$ is *not* in between that based on respectively $q = 1.0$ and $q = 1.4$, as one might tend to expect. According to figure 8*b*, the value of q also affects the critical groove orientations. It is found that the predicted critical groove orientations for the latent hardening sheets ($q > 1.0$) are quite different to those for the isotropic hardening sheet ($q = 1.0$), especially near balanced biaxial tension. The differences in the calculated critical groove angles between $q = 1.2$ and $q = 1.4$ are small.

It is worthwhile to point out that the study of above cases, with different values of q and same value of n, can reveal the effect of latent hardening only to some extent. The reason for this is that these different sets of hardening parameters actually represent different materials, because their stress responses (e.g. the predicted uniaxial stress–strain curves) are quite different. Therefore, we now consider the following three different combinations of n and q: ($q = 1.0$, $n = 0.245$), ($q = 1.2$, $n = 0.229$) and ($q = 1.4$, $n = 0.214$). These three sets of hardening parameters give virtually identical uniaxial tensile response (in the rolling direction), as shown in figure 9. The corresponding predicted FLDs with $f = 0.997$ are presented in figure 10. It is found that the differences in predicted FLDs between the latent hardening ($q = 1.2$ or $q = 1.4$) and the isotropic hardening ($q = 1.0$) are much more significant than that in figure 8*a*, especially near balanced biaxial tension. The predicted critical groove orientations are found to be similar to those shown in figure 8*b*.

These results indicate that the activated slip systems for a given strain path ($\rho =$ const.) are different in sheets with different hardening parameters q, so that the final textures should be expected to be different too. Furthermore, it appears that these

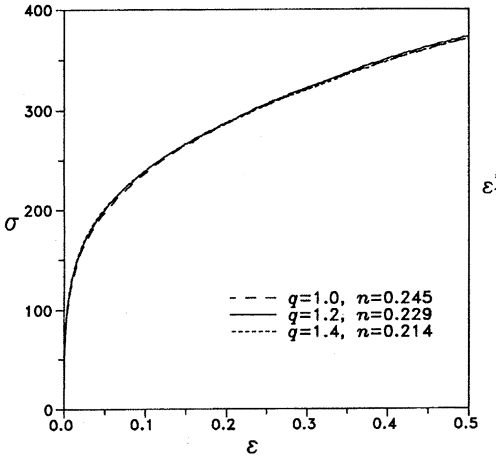

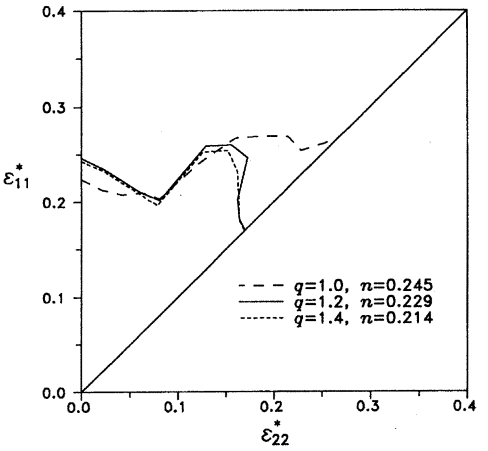

Figure 9. (Left) Stress responses to uniaxial tension of an initially textured sheet for three different sets of hardening parameters.

Figure 10. (Right) Predicted FLDs, based on three different sets of hardening parameters, for an initially textured sheet.

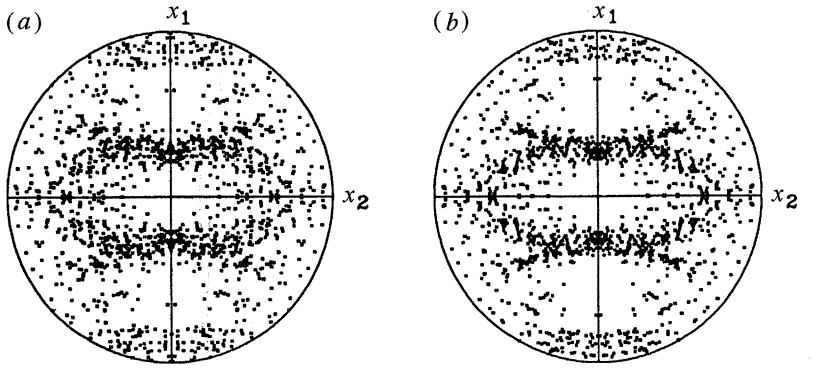

Figure 11. Calculated textures at necking for an isotropic hardening sheet ($q = 1.0$, $n = 0.245$) under in-plane plane-strain tension: (a) outside; and (b) inside the groove, with $f = 0.997$ and an initial texture shown in figure 2a.

differences may not be the same near balanced biaxial tension and near in-plane plane-strain tension ($\rho = 0$). Figure 11 shows the calculated textures at necking for an isotropic hardening sheet ($q = 1.0$, $n = 0.245$) under in-plane plane-strain tension. The texture outside the band at necking is a typical plane-strain tension texture (figure 11a). As expected, the texture inside the groove (figure 11b) is stronger than that outside the groove. For a latent hardening sheet with $q = 1.4$ and $n = 0.214$, we find from figure 12a that the predicted texture outside the groove at necking is considerably sharper than that for the isotropic hardening sheet in figure 11a. One may attribute this to the fact that the predicted limit strain ε^*_{11} for the latent hardening sheet is 0.243, while it is only 0.224 for the isotropic hardening sheet. However, the difference in ε^*_{11} alone cannot induce such a large difference observed in the predicted textures; this large difference is mainly due to the latent hardening. This point of view is supported by comparing figures 13 and 14, which present the simulated textures for isotropic and anisotropic hardening sheets, respectively, under balanced biaxial tension at necking. It is observed that the texture outside the groove for the latent hardening sheet at necking (figure 14a) is much stronger

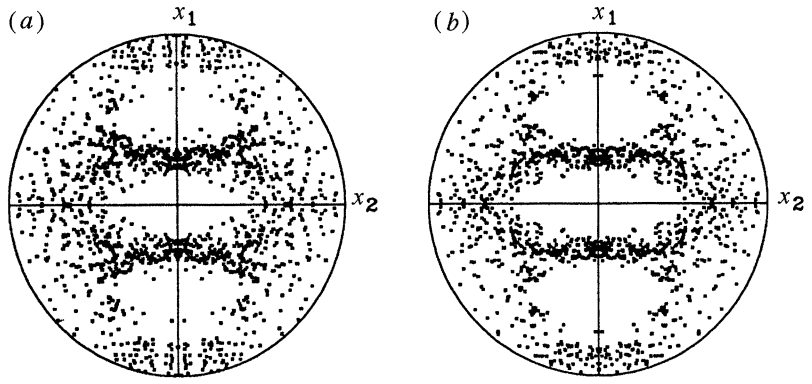

Figure 12. Calculated textures at necking for a latent hardening sheet ($q = 1.4$, $n = 0.214$) under in-plane plane-strain tension: (*a*) outside; and (*b*) inside the groove, with $f = 0.997$ and an initial texture shown in figure 2*a*.

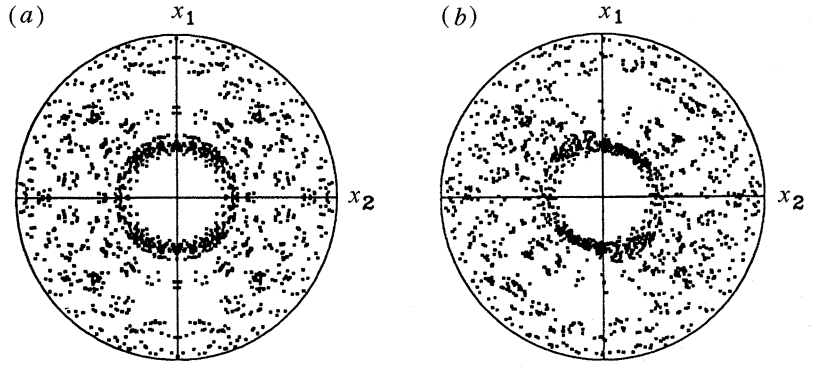

Figure 13. Calculated textures at the onset of necking for an isotropic hardening sheet ($q = 1.0$, $n = 0.245$) under balanced biaxial tension: (*a*) outside; and (*b*) inside the groove, with $f = 0.997$ and an initial texture shown in figure 2*a*.

than that for the isotropic hardening sheet (figure 13*a*). Since the limit strains ($\varepsilon^*_{11} = \varepsilon^*_{22} = 0.169$) for the latent hardening sheet are much smaller than the limit strains ($\varepsilon^*_{11} = \varepsilon^*_{22} = 0.265$) for the isotropic hardening sheet, the difference observed in the predicted textures must be completely due to the effect of latent hardening. The rolling direction of the simulated texture for isotropic hardening sheet inside the groove (figure 13*b*) is found to be inclined at about 45°, since the critical groove orientation is in this case inclined at an angle $\psi_{\mathrm{I}} = 45°$. Figure 13*b* also indicates that shear strain components induced inside the groove become significant.

Although the material inside the groove tends towards a plane-strain deformation state irrespective of the deformation imposed outside the groove, the simulated textures inside the groove (e.g. figures 13*b* and 14*b*) only show a very weak plane strain tension texture. The reason for this is that computations were stopped at the onset of necking (when $\dot{\varepsilon}^{\mathrm{b}}/D_{11} \geqslant 10^5$), and at that instant the deformation inside the groove has not yet become very large compared to the applied deformation. In some of the cases, we continued the computations beyond neck initiation, and we found that as the applied deformations concentrated in the groove, the material inside the groove reached a plane-strain deformation state.

So far, all computations performed on the initially textured sheet have shown a dip near in-plane plane-strain tension ($\rho \approx 0$) in the predicted FLDs. We noted that

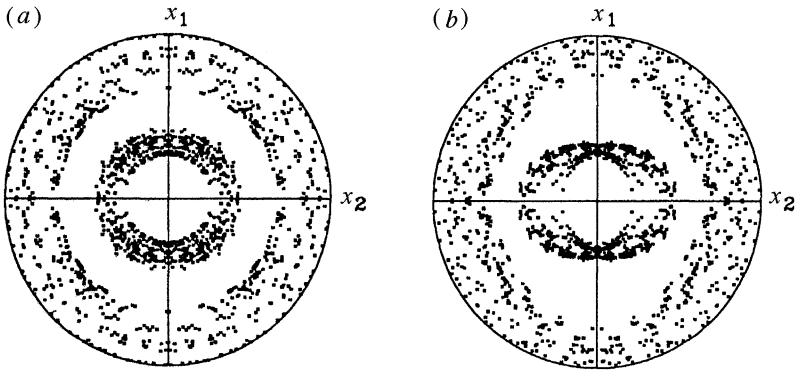

Figure 14. Calculated textures at the onset of necking for a latent hardening sheet ($q = 1.4$, $n = 0.214$) under balanced biaxial tension: (a) outside; and (b) inside the groove, with $f = 0.997$ and an initial texture shown in figure 2a.

this is a feature that has also been observed experimentally, but never revealed in numerical simulations by other researchers who also apply crystal plasticity models in their FLD analyses (e.g. Zhou & Neale 1995; Barlat 1989). The question then arises: where does the dip come from? One possibility is the effect of crystal elasticity, since one of the important differences between our approach and others mentioned above is that the elastic effect is included in our analyses but is excluded in the others. To examine the effect of crystal elasticity on the FLD, we consider a 'rigid'-plastic material with very large elastic constants C'_{11}, C'_{12} and C'_{44} that are all a factor 100 larger than the corresponding values of C_{11}, C_{12} and C_{44}, but with all other parameters, such as hardening parameters, kept unchanged. The term 'rigid' plastic is used here because the stress–strain curve of this material is almost identical to that of the corresponding ideal rigid-plastic material. The predicted FLDs are presented in figure 15a. It is clear that the dip is not observed in the simulated FLD for the 'rigid'-plastic sheet. Thus, it seems that it is the very large elastic stiffness that eliminates the dip. Conversely, figure 15a indicates that increasing the elastic modulus of a sheet metal can improve its formability. The effect of crystal elasticity on the simulated critical groove orientations is observed in figure 15b.

(e) *An example for a rolled aluminium alloy sheet*

At this stage, it might be of interest to compare simulated and measured FLDs. As an example, we consider a real aluminium alloy sheet with its measured initial texture being that already shown in figure 2a. The strain rate sensitivity $m = 0.002$ is suggested by the material producer, while the slip system reference plastic shearing rate is taken as before, $\dot{\gamma}_0 = 0.001\ \mathrm{s}^{-1}$. Also, the crystal elastic constants are taken identical to the values used previously. They are typical for an aluminium alloy. We assume isotropic hardening ($q = 1$) and estimate the hardening parameters in the crystal plasticity constitutive model by curve-fitting numerical simulations of uniaxial tension (in the rolling direction) to corresponding experimental data. From this procedure we find: $\tau_0 = 22$ MPa, $h_0/\tau_0 = 181.82$ and $n = 0.245$. Figure 16 shows that the curve-fit is quite good.

In the simulations, the value of the initial imperfection parameter was taken as $f = 0.997$, which was estimated by fitting the limit strain of in-plane plane-strain tension ($\rho = 0$) to the test result for the same sheet. It is noted that this high value is consistent with Barlat's work (Barlat *et al.* 1984; Barlat & Jalinier 1985), where

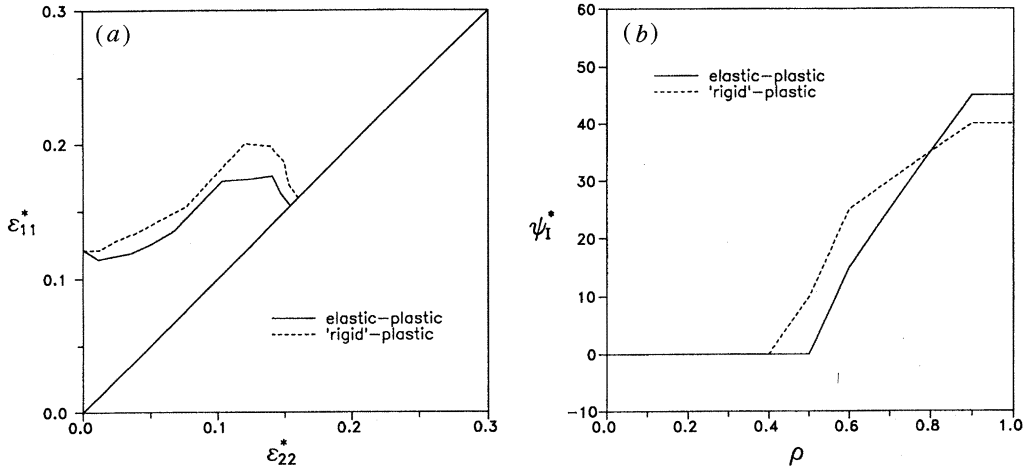

Figure 15. Influence of crystal elastic properties on: (*a*) the predicted FLDs; and (*b*) the the predicted critical groove orientations for an initially textured sheet.

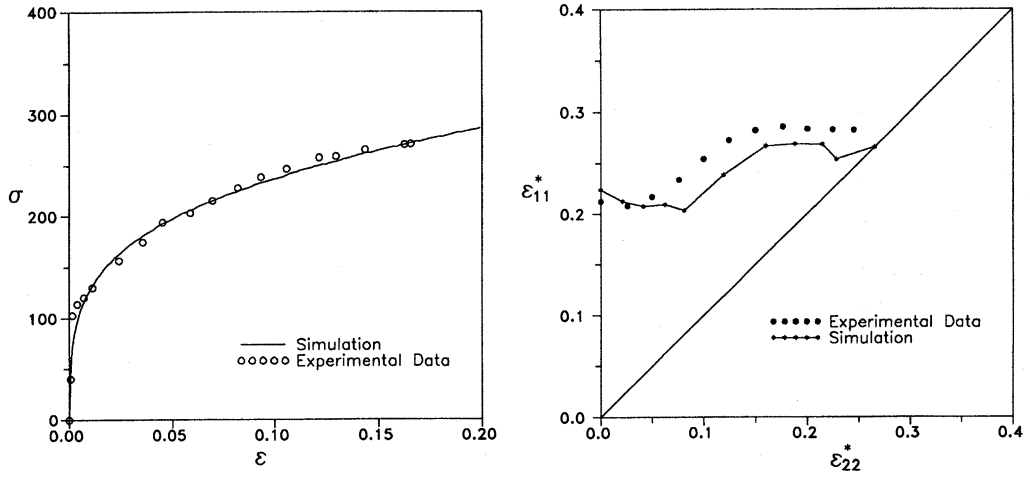

Figure 16. (Left) Tensile stress response in uniaxial tension for an aluminium alloy sheet with its initial texture given in figure 2*a*.
Figure 17. (Right) Predicted and measured FLDs for the aluminium alloy sheet of figure 16.

the initial imperfection was assumed to result from homogeneously distributed microcavities. Using a physical description of the cavities, they estimated imperfection values of about 0.996 or 0.997. Figure 17 shows the simulated and measured FLDs. It is seen that the agreement between the simulated and measured FLDs is reasonable, and the shape of the experimental FLD is predicted quite well.

5. Conclusion

In this paper, we have analysed FLDs based on the elastic–viscoplastic Taylor-type polycrystal plasticity model developed by Asaro & Needleman (1985). The effects of initial imperfection intensity and orientation, initial distribution of grain orientations, crystal elasticity, strain rate sensitivity, single slip hardening and latent hardening on the FLD have been discussed in detail.

The influence of some of the material properties on the FLD are easy to assess. For example, an increasing strain-rate sensitivity value, m, shifts the FLD towards higher values of major limit strain ε_{11}^{*}. The effect of the single slip hardening parameter, n, is similar. These trends are completely analogous to the well-known effects of hardening and rate-sensitivity in phenomenological plasticity (e.g. Hutchinson & Neale 1978). Although the value of the initial imperfection parameter, f, cannot be directly measured by physical experiments, its influence on the FLD can be examined numerically. As expected, the smaller the imperfection, the larger the major limit strain ε_{11}^{*}.

On the other hand, the effect of latent hardening on the FLD is quite complex. In general, latent hardening has a strong effect on the currently activated slip systems, which determine texture evolution and thus affect the FLD. What renders this phenomenon even more complicated is that the effect of the latent or anisotropic hardening is dependent on the strain path. Therefore, changing the latent hardening parameter, q, results in changes of the shape of the FLD. It should be noted, however, that all results reported here were based on the simple power-law single-slip hardening model. In order to further assess the influence of latent hardening, it may be necessary to consider other hardening models, such as the recently proposed Bassani–Wu (Bassani & Wu 1993) model. The Bassani–Wu model is a more physically motivated hardening model, and is capable of predicting a number of experimentally observed phenomena that other models, such as the hardening model adopted here, cannot represent. For example, it has been found that only the Bassani–Wu hardening-based Taylor-type polycrystal plasticity model qualitatively predicts the experimental shapes of the normal stress curve in fixed-end torsion and the axial-strain curve in free-end torsion (Wu *et al.* 1996). However, the Bassani–Wu model involves many material parameters to be specified experimentally, so that more experimental data on sheet materials would be required.

Unexpectedly, the effect of crystal elasticity on the FLD was revealed to be important. Previous works based on phenomenological plasticity models suggested that the predicted FLDs are not sensitive to elastic properties of the materials. Consequently, elasticity has been neglected in most FLD analyses, for instance, in Barlat (1987), Van Houtte & Tóth (1993), Ratchev *et al.* (1994) and in Zhou & Neale (1995). Our numerical results, however, have clearly shown the importance of elasticity on FLDs. Details aside, 'rigid' plasticity eliminates the dip in the FLD near in-plane plane-strain tension, observed in the corresponding more realistic elastic–plastic FLD analyses. For a given initial texture, it is the elastic effect which determines the shape of the FLD near in-plane plane-strain tension. It is apparently impossible for an FLD analysis neglecting elasticity to reproduce the dip observed in the experimental determined FLDs. To our knowledge, the present result is the first which predicts this dip. Our analyses also indicated that increasing the elastic modulus of a sheet metal improves its formability.

The importance of the effect of the shape of the yield surface on the FLD has been recognized for a long time. As pointed out before, in the crystal plasticity FLD analysis carried out here, the shape of the yield surface for a sheet metal is determined by the initial texture and its evolution. Consequently, the initial texture is one of the most important effects on the FLD. Our numerical study on the effect of initial texture on the FLD, shown in figure 5, suggests the possibility of designing forming processes that led to textures that enhance the resistance to localization for specified strain paths.

The predicted FLDs have been compared with experimental data for an aluminium alloy sheet. The predictions were based on an experimentally measured initial texture, while the values of the hardening parameters in the constitutive model were estimated by curve-fitting numerical simulation of uniaxial tension to corresponding experimental data. In general, the agreement is reasonable, and the shape of the experimental FLD is predicted reasonably well. The differences between the calculated and experimental FLDs could be due to the fact that we simulated in-plane stretching deformation processes, while the experimental data were obtained from hemispherical punch stretching tests. In punch tests, there are compressive stresses normal to the sheet, frictional shear stresses, and sheet curvature. Furthermore, the strain paths are not necessary proportional. These complicating factors have not been accounted for in our analyses. Furthermore, it has been found that the measured FLDs from in-plane stretching lie below the corresponding punch-stretching FLDs (Ghosh & Hecker 1974). Based on this observation, the agreement between the calculated and experimental FLDs can be considered to be quite good. However, it was found that the predicted FLDs are not very smooth. The reason for this is that the measured initial texture was represented by only 408 grains. For an initially anisotropic FCC polycrystal, using only around 400 grains is probably not sufficient to accurately discretize the initial texture. However, our predictions with 408 grains do appear to capture the key features of the FLD for the aluminium alloy sheet studied.

An important point that has not been addressed is the effect of changing strain paths on FLDs. During an actual forming operation, a material element may undergo considerably large changes in strain path, and these changes may significantly alter the forming limits. The ability to include path changes in FLD calculations is important because the number of potentially significant changes is too great to be thoroughly covered by experiments and because calculations allow general trends to be explored over a large range of variables. Investigations of the effect of changing-strain paths on the FLD by means of the numerical tool presented here will be reported elsewhere.

This work was supported by the Natural Sciences and Engineering Research Council of Canada (NSERC) and the Government of the Province of Quebec (Programme FCAR). P.D.W. is grateful for the NSERC Canada International Fellowship which supported his postdoctoral position at the Université de Sherbrooke.

References

Asaro, R. J. & Needleman, A. 1985 Texture development and strain hardening in rate dependent polycrystals. *Acta Metall.* **33**, 923–953.

Barlat, F. 1987 Crystallographic texture, anisotropic yield surfaces and forming limits of sheet metals. *Mater. Sci. Tech.* **91**, 55–72.

Barlat, F. 1989 Forming limit diagrams—predictions based on some microstructural aspects of materials. In *Forming limit diagrams: concepts, methods and applications* (ed. R. H. Wagoner, K. S. Chan & S. P. Keeler), pp. 275–301. Warrendale, PA: The Minerals, Metals & Materials Society.

Barlat, F. & Jalinier, J. M. 1985 Formability of sheet metal with heterogeneous damage. *J. Mater. Sci.* **20**, 3385–3399.

Barlat, F. & Richmond, O. 1987 Prediction of tricomponent plane stress yield surfacees and associated flow and failure behaviour of strongly textured FCC polycrystalline sheets. *Mater. Sci. Tech.* **95**, 15–29.

Barlat, F., Barata da Roberts, A. & Jalinier, J. M. 1984 Influence of damage on the plastic instability of sheet metal under complex strain path. *J. Mater. Sci.* **19**, 4133–4137.

Bassani, J. L. & Wu, T. Y. 1991 Latent hardening in single crystals. II. Analytical characterization and predictions. *Proc. R. Soc. Lond.* A **435**, 21–41.

Bassani, J. L., Hutchinson, J. W. & Neale, K. W. 1979 On the prediction of necking in anisotropic sheets. *Metal forming plasticity* (ed. H. Lippman), pp. 1–13. Berlin: Springer.

Chan, K. S. 1989 Marciniak–Kuczynski approach to calculating forming limit diagrams. In *Forming limit diagrams: concepts, methods and applications* (ed. R. H. Wagoner, K. S. Chan & S. P. Keeler), pp. 73–110. Warrendale, PA: The Minerals, Metals & Materials Society.

Ferron, G. & Molinari, A. 1989 Mechanical and physical aspects of sheet-metal ductility. In *Forming limit diagrams: concepts, methods and applications* (ed. R. H. Wagoner, K. S. Chan & S. P. Keeler), pp. 111–151. Warrendale, PA: The Minerals, Metals & Materials Society.

Ghosh, A. K. & Hecker, S. S. 1974 Stretching limits in sheet metals: in-plane versus out-of-plane deformation. *Metall. Trans.* **5**, 2161–2164.

Giessen, E. Van der & Neale, K. W. 1993 Analysis of the inverse Swift effect using a rate-sensitive polycrystal model. *Comp. Meth. Appl. Mech. Engng* **103**, 291–313.

Hecker, S. S. 1975 Formability of aluminum alloy sheet. *J. Engng Mater. Tech.* **97**, 66–73.

Hill, R. 1952 On discontinuous plastic states with special reference to localized necking in thin sheets. *J. Mech. Phys. Solids* **1**, 19–30.

Houtte, P. Van & Tóth, L. S. 1993 Generalization of the Marciniak–Kuczynski defect model for predicting forming limit diagrams. In *Advances in engineering plasticity and its applications* (ed. W. B. Lee), pp. 1013–1020. New York: Elsevier.

Hutchinson, J. W. & Neale, K. W. 1978 Sheet necking. II. Time independent behaviour. III. Strain-rate effects. In *Mechanics of sheet metal forming* (ed. K. P. Koistinen & N.-M. Wang), pp. 127–153, 269–285. New York: Plenum.

Lege, D. J., Barlat, F. & Brem, J. C. 1989 Characterization and modeling of the mechanical behaviour and formability of a 2008-T_4 sheet sample. *Int. J. Mech. Sci.* **31**, 549–563.

Lian, J., Barlat, F. & Baudelet, B. 1989 Plastic behaviour and stretchability of sheet metals. II. Effect of yield surface shape on sheet forming limit. *Int. J. Plast.* **5**, 131–147.

Marciniak, Z. & Kuczynski, K. 1967 Limit strains in the processes of stretch-forming sheet metals. *Int. J. Mech. Sci.* **9**, 609–620.

Neale, K. W. & Chater, E. 1980 Limit strain predictions for strain-rate sensitive anistropic sheets. *Int. J. Mech. Sci.* **22**, 563–574.

Peirce, D., Asaro, R. J. & Needleman, A. 1983 Material rate dependence and localized deformation in crystalline solids. *Acta Metall.* **31**, 1951–1976.

Qiu, Y., Neale, K. W., Makinde, A. & MacEwen, S. R. 1995 Numerical modelling of metal formability using polycrystal plasticity. In *Simulation of materials processing: theory, methods and applications* (ed. S. Shen & P. R. Dawson), pp. 327–331. Rotterdam: Balkema.

Ratchev, P., Houtte, P. Van, Verlinden, B., De Smet, P., Neutjens, P., Baartman, R. & Drent, P. 1994 Prediction of forming limit diagrams of Al–Mg rolled sheet taking texture into account. *Textures Microstruct.* **22**, 219–231.

Stören, S. & Rice, J. R. 1975 Localized necking in thin sheets. *J. Mech. Phys. Solids* **23**, 421–441.

Tvergaard, V. & Needleman, A. 1993 Shear band development in polycrystals. *Proc. R. Soc. Lond.* A **443**, 547–562.

Wilson, D. V., Roberts, W. T. & Rodrigues, P. M. B. 1981 Effect of grain anisotropy on limit strains in biaxial stretching: Part I. Influence of sheet thickness and grain size in weakly textured sheets. *Metall. Trans.* A **12**, 1595–1611.

Wu, P. D., Neale, K. W. & Giessen, E. Van der 1996 Simulation of the behaviour of FCC polycrystals during reversed torsion. *Int. J. Plast.* **12**, 1199–1219.

Zhou, Y. & Neale, K. W. 1995 Predictions of forming limit diagrams using a rate-sensitive crystal plasticity model. *Int. J. Mech. Sci.* **37**, 1–20.

Received 6 September 1996; revised 24 January 1997; accepted 7 March 1997